Materials
Advances

ROYAL SOCIETY
OF CHEMISTRY

PAPER

View Article Online
View Journal | View Issue

Check for updates

Cite this: *Mater. Adv.*, 2026, 7, 1621

Visible light-driven photocatalytic properties of polyphosphodiester-protected silver nanocomposites

Thanaporn Jullabuth,[a] Yota Okuno,[bc] Hideya Kawasaki,[bc] Satoshi Ichikawa[d] and Yasuhiko Iwasaki *[bc]

Silver nanocomposites are used to develop photocatalysts for various environmental, energy, and biomedical applications. However, the stability, biocompatibility, and performance of these colloids for practical applications need further improvement. Herein, silver nanocomposites protected with polyphosphodiesters (PPDEs) were successfully synthesized. A conjugate was prepared by varying the ratio of phosphodiesters to silver acetate, which were then exposed to visible light to form the silver nanocomposites, known as PEP·Na_aAg_b-l (a and b correspond to the ratio of Na^+ and Ag^+ in the feed). Then, the stability, photocatalytic activity, and recyclability of the colloids were evaluated. The spectral changes observed before and after irradiation confirmed the formation of photogenerated nanocomposites. The morphology of PEP·Na_aAg_b-l was characterized by transmission electron microscopy (TEM), high-resolution transmission electron microscopy (HRTEM), selected area electron diffraction (SAED), and X-ray photoelectron spectroscopy (XPS). The silver nanocomposites efficiently degraded rhodamine B (RhB) under visible light, with the degradation efficiency of PEP·Na_5Ag_1-l reaching 89% (k = 5.12 × 10^{-2} min^{-1}), indicating their photocatalytic performance. These nanocomposites achieved over 87% degradation of RhB even after six cycles, demonstrating their recyclability. The stability and recyclability of the colloids were reinforced by the polyphosphodiester. The role of specific reactive oxygen species (ROS) was explored by the conventional scavenger approach. The silver nanocomposites play a crucial role in the heterojunction, enhancing not only light harvesting but also increasing the capacity for electron acceptance and suppressing electron–hole recombination.

Received 8th November 2025,
Accepted 23rd December 2025

DOI: 10.1039/d5ma01295c

rsc.li/materials-advances

1. Introduction

Numerous studies have explored the design and synthesis of highly efficient photocatalysts for several applications, such as environmental purification,[1–3] sustainable energy utilization,[4,5] and medical engineering.[6–9] In the 1970s, Fujishima and Honda discovered the ability of titanium dioxide (TiO_2) to drive photoelectrochemical water splitting under ultraviolet light,[10] which revolutionized the photocatalytic industry. The unique properties of TiO_2, including its chemical stability, electronic structure, and low cost[11] make it an excellent photocatalyst. However, its applications are constrained by its wide band gap energy (3.0–3.2 eV), which could utilize ~5% of the solar energy.[12,13] To promote the efficiency of solar energy utilization, selecting materials with an absorption range that extends into the visible-light spectrum is a practical solution.

Recently, silver-based materials have garnered attention.[14–16] Typically, silver(II) oxide (AgO), a p-type semiconductor with an optical band gap of 0.93–1.2 eV,[17,18] displays superior light absorption. Silver(I) oxide (Ag_2O) is another outstanding photocatalyst, which can degrade persistent organic pollutants.[19,20] Nevertheless, the practical applications of single-component photocatalysts are limited by rapid electron–hole recombination and poor stability.[21,22] Modifying their physicochemical and optical characteristics *via* heterojunction construction and cocatalyst integration[23] can help overcome these issues. Metal nanocomposites incorporating gold, platinum, and silver are being increasingly explored due to their electron trapping and optical properties, which facilitate efficient charge separation. Particularly, silver nanocomposites exhibit a strong surface plasmon resonance effect, which enhances their photocatalytic

---

[a] *Graduate School of Science and Engineering, Kansai University, 3-3-35 Yamate-cho, Suita-shi, Osaka, 564-8680, Japan*
[b] *Department of Chemistry and Materials, Faculty of Chemistry, Materials and Bioengineering, Kansai University, 3-3-35 Yamate-cho, Suita-shi, Osaka, 564-8680, Japan. E-mail: yasu.bmt@kansai-u.ac.jp; Fax: +81-6-6368-0090; Tel: +81-6-6368-0090*
[c] *ORDIST, Kansai University, 3-3-35 Yamate-cho, Suita-shi, Osaka, 564-0836, Japan*
[d] *Research Center for Ultra-High Voltage Electron Microscopy, Osaka University, Ibaraki, 567-0047, Japan*

performance under visible light.[24,25] Silver nanocomposites can also trigger the recombination of electron–hole pairs, acting as electron sinks due to the Schottky barrier.[26,27] Recent studies have demonstrated the remarkable photocatalytic performance of silver cocatalysts, including silver nanocomposites such as Ag/Ag_2O,[28,29] Ag/AgCl,[30,31] Ag/Ag_3PO_4,[32] and Ag/AgO/Ag_2O,[33] due to their narrow bandgap and excellent electrical conductivity.[34,35]

Poly(ethylene sodium phosphate) (PEP·Na) is a polyphosphodiester (PPDE) that exhibits excellent water solubility (>200 mg ml^{-1}). A PPDE is formed through a reaction between a polyphosphotriester (PPTE) and trimethylamine, resulting in a polysalt, which was then treated with cation-exchange resin and neutralization.[36] The modification of PPTE's side chains into PPDE allows precise tuning of the polymer's properties.[37] Studies have explored the role of PEP·Na in various applications, including drug delivery,[38,39] osteoporosis prevention,[40] and protein conjugation.[41] However, the effect of exchanging Na^+ ions with other ions on the photocatalytic performance of these compounds remains unexplored, which might lead to novel applications.

Herein, we aimed to synthesize silver nanocomposites protected with PPDEs *via* visible-light irradiation. The structural, morphological, and optical properties of the synthesized material were thoroughly investigated. The results showed that these nanocomposites exhibited effective photocatalytic activity for rhodamine B (RhB) degradation under visible light and enhanced dispersibility due to the properties of PPDEs. Furthermore, the silver nanocomposites retained over 87% efficiency in dye degradation even after six cycles, highlighting their recyclability.

2. Experimental section

2.1. Materials

2-Chloro-2-oxo-1,3,2-dioxaphosphalane (COP) was obtained from NOF Co., Ltd (Tokyo, Japan). 2-Methoxy-2-oxo-1,3,2-dioxaphospholane (MP) was distilled under reduced pressure and stored under argon at 4 °C until further use.[42] The cation-exchange resin Amberlite IR120 was supplied by Merck KGaA (Darmstadt, Germany). A 30% aqueous solution of trimethylamine was purchased from Nacalai Tesque, Inc. (Osaka, Japan). 1,8-Diazabicyclo[5,4,0]-undec-7-ene (DBU) was purchased from Sigma-Aldrich (Saint Louis, USA). Methanol, 2,6-dimethylpyridine (2,6-lutidine), toluene, chloroform-D 99.8% (contains 0.05 vol% TMS), benzyl alcohol, acetic acid, diethyl ether, sodium hydroxide (NaOH), fuming nitric acid, and silver acetate (CH_3COOAg) were purchased from FUJIFILM Wako Pure Chemical Inc. (Osaka, Japan).

2.2. Preparation of silver nanocomposites protected with PPDEs

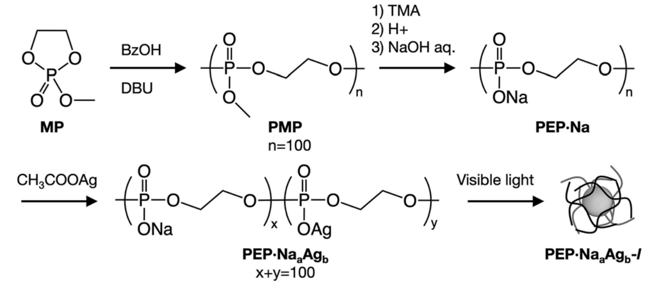

Fig. 1 Synthesis of PEP·Na_aAg_b-l.

First, we synthesized PEP·Na (Fig. 1). Briefly, 45 mmol of MP was mixed with 0.45 mmol of benzyl alcohol to facilitate polymerization. Then, DBU was added under an argon gas atmosphere. After stirring the mixture in an ice bath at 0 °C, methanol was added to reduce viscosity. After quenching DBU with acetic acid, the product was purified and reprecipitated from diethyl ether. Trimethylamine was used for quaternization, followed by a reaction with cation-exchange resin. Subsequently, the solution was filtered to remove the cation-exchange resin, and sodium hydroxide was added as a neutralizing agent. Then, the polymer solution was dialyzed for three days using a membrane with a molecular weight cut-off of 1000 (Spectra/Por®, Spectrum Laboratories, Inc., Rancho Dominguez, CA, USA), immersed in ultrapure water. The dialyzed solution was freeze-dried, yielding PEP·Na as a colorless solid.

Then, 200 mg of PEP·Na was mixed with CH_3COOAg at room temperature for 60 minutes. The mol ratio of phosphodiester unit (EP·Na) to CH_3COOAg was adjusted to 1 : 1, 2 : 1, and 5 : 1. In PEP·Na_aAg_b, a/b corresponds to the feeding ratio of EP·Na and CH_3COOAg. So, the PEP·Na_1Ag_1, PEP·Na_2Ag_1, and PEP·Na_5Ag_1 represent samples before exposure to the visible light. After dialysis for two days and freeze-drying, a gray colored solid was obtained. The ^{1}H-NMR spectra of each sample were obtained using a JNM-ECZ400 instrument (JEOL Ltd, Tokyo, Japan). The weight-average molecular weight (M_w) and molecular weight distribution were determined by JASCO gel-permeation chromatography (GPC; JASCO Corporation, Tokyo, Japan) using a calibration curve based on linear polyethylene glycol (PEG) standards. The elemental composition was precisely quantified using inductively coupled plasma-optical emission spectrometry (ICP-OES; Shimadzu Corporation, Kyoto, Japan), ensuring the accuracy of the silver content conjugated with PPDEs.

In the final step, we irradiated each sample with visible light at 83 mW cm^{-2} for 60 minutes to form silver nanocomposites. Subsequently, the sample was freeze-dried to keep it in a solid state. After exposure to visible light, each sample is labeled as "light." Therefore, PEP·Na_1Ag_1-l, PEP·Na_2Ag_1-l, and PEP·Na_5Ag_1-l represent samples already exposed to the light.

2.3. Characterization of silver nanocomposites protected with PPDEs

The absorbance was measured using JASCO V-650 and V-730 UV-Vis spectrophotometers (JASCO Corporation, Tokyo, Japan) in the range of 200–600 nm and 200–1100 nm, respectively. The wavelength accuracy of both the JASCO V-650 and JASCO V-730 instruments was ±0.2 nm, and the spectral bandwidth used for all measurements was 1.0 nm. Detailed morphological and crystallographic analyses were performed using transmission electron microscopy (TEM; JEM-1400, JEOL Ltd, Tokyo, Japan), operated at an accelerating voltage of 100 kV. TEM images of the synthesized material were used to determine the size and shape. A drop of the diluted sample was placed onto a carbon-coated copper grid. After leaving it for 10 minutes, the liquid fraction was carefully removed using filter paper. Particle sizes were determined from TEM images using ImageJ. The images were calibrated using the scale bar, and the diameter of 100 individual particles was manually measured. The lattice parameter was analyzed using selected area electron diffraction (SAED) and a high-resolution transmission electron microscope (HRTEM; ARM 200F, JEOL Ltd, Tokyo, Japan), operated at 200 kV. The result was then used to identify the crystalline structure using ReciPro software.[43] A Zetasizer (Malvern Instruments, Worcestershire, UK) was employed to determine the average size and zeta potential, with particle size measurements better than ±2% on NIST traceable latex standards. X-ray photoelectron spectroscopy (XPS) measurements were performed using a Kratos AMICUS/ESCA 3400 spectrometer (Kratos Analytical Ltd, Manchester, UK), equipped with a Mg anode X-ray source (1253.6 eV), which enabled detailed analysis of surface chemical states. The XPS binding energies were accurately calibrated using the phosphorus (P_{2p} = 133.0 eV), ensuring reliability in the characterization of the silver nanocomposites protected with PPDEs.

2.4. Photocatalytic activity

The photocatalytic activity was examined using 0.25 mg ml^{-1} (250 ppm) of the silver nanocomposites protected with PPDEs, combined with 6.9×10^{-6} M of RhB (3.3 ppm). The RhB concentration was adjusted to ensure reliable linearity in the measurements. Then, the mixture was exposed to visible light at 83 mW cm^{-2}. To calculate the C/C_0 ratio and first-order kinetics, the solution was collected at various intervals, and the supernatant was separated *via* centrifugation at 15 000 rpm for 5 minutes before analysis. The degradation of RhB was quantitatively analyzed by measuring the decreased maximum absorption peak at 554 nm using a UV-Vis spectrophotometer. A RhB solution without the silver nanocomposites was used as the control to negate the influence of light on the dye. The degradation of RhB follows a pseudo-first-order kinetic model with respect to the reaction time:

$$-\ln(C_t/C_0) = k \times t \tag{1}$$

Here, C_0 and C_t represent the initial concentrations of RhB and those at various time intervals, respectively. k (min^{-1}) represents the apparent rate constant of the reaction.

2.5. Free radical scavenging experiment

The reactive species, such as h$^+$, $^\bullet$OH, and $O_2^{-\bullet}$ radicals, were identified using free radical scavenging agents specific to each species, including triethanolamine (TEOA), 2-propanol, and *p*-benzoquinone (*p*-BQ), respectively. The RhB degradation efficiency was compared with that of the sample with no scavenger.

2.6. Stability of silver nanocomposites protected with PPDEs

A 0.25 mg ml^{-1} sample was mixed with ultrapure water, and RhB was added to achieve a final concentration of 3.3 ppm in a total volume of 200 µl. After exposure to visible light for 90 minutes, the supernatant was separated by centrifuging at 15 000 rpm for 15 minutes. The RhB degradation efficiency (%) is calculated as $(A_0 - A_t)/A_0 \times 100$, where A_0 represents the initial absorbance and A_t represents the absorbance after decomposition.

3. Results and discussion

3.1. Preparation of silver nanocomposites protected with PPDEs

The ring-opening polymerization of MP resulted in PMP, which was demethylated to yield PEP·Na.[44,45] The average polymerization degree of both PMP and PEP·Na was 100, and their molecular weights (M_w), measured using GPC, were 11.0×10^3 and 13.5×10^3, respectively. The yield of PEP·Na, calculated from the integration of ^{1}H NMR spectra, was determined to be 96.5%. Both PMP and PEP·Na exhibited high water solubility and the capacity to function as electron acceptors, making them efficient supporting materials in metal-containing catalysts.

The samples were synthesized by adjusting the ratio of [PEP·Na] : [CH_3COOAg] to 1 : 1 (PEP·Na_1Ag_1), 2 : 1 (PEP·Na_2Ag_1), and 5 : 1 (PEP·Na_5Ag_1), in which CH_3COOAg was the precursor of Ag$^+$. The characteristics of PEP·Na_aAg_b are presented in Table 1. The ICP results show that the Ag concentrations of PEP·Na_1Ag_1, PEP·Na_2Ag_1, and PEP·Na_5Ag_1 were 0.96, 0.79, and 0.36 ppm, respectively. Accordingly, the actual molar ratios of [EP·Na] : [EP·Ag] for the aforementioned samples were 0.28 : 1, 0.50 : 1, and 2.72 : 1, respectively.

During ion exchange, Na$^+$ ions were replaced with Ag$^+$ ions to yield PEP·Na_aAg_b (Fig. 2(a)). Upon exposure to visible light, the Ag$^+$ ions produced may react with oxygen embedded in the polymer, forming stable oxides, such as AgO and Ag_2O. Since the formation of these oxides is non-selective, a mixture of AgO and Ag_2O might be present[46] (Fig. 2(b)). Simultaneously, the absorbed photons provide energy to excite electrons from the

Table 1 Characterization of PEP·Na_aAg_b

Sample	[EP·Na] : [CH_3COOAg] (mol)	M_n[a] ($\times 10^3$)	M_w[a] ($\times 10^3$)	M_w/M_n[a]	Na conc.[b] (ppm)	Ag conc.[b] (ppm)	[EP·Na] : [EP·Ag] (mol)
PEP·Na_1Ag_1	1 : 1	10.6	13.4	1.26	0.17	0.96	0.28 : 1
PEP·Na_2Ag_1	2 : 1	10.5	13.3	1.26	0.25	0.79	0.50 : 1
PEP·Na_5Ag_1	5 : 1	11.1	14.9	1.34	0.62	0.36	2.72 : 1

[a] Determined by GPC. [b] Determined by ICP-OES.

valence band (VB) to the conduction band (CB).[47,48] This process generates an electron–hole pair, where the excited electrons in the CB can reduce Ag^+ ions to form silver nanocomposites. Along with its primary role as an electron acceptor, Ag^+ can also interact with holes (h^+) left in VB to produce high-valent silver species, as shown in eqn (2)–(4).[49]

$$\mathrm{PEP{\cdot}Na_aAg_b} + h\nu \rightarrow \mathrm{e^-} + \mathrm{h^+} \tag{2}$$

$$\mathrm{Ag^+} + \mathrm{e^-} \rightarrow \mathrm{Ag^0} \tag{3}$$

$$\mathrm{Ag^+} + \mathrm{h^+} \rightarrow \mathrm{Ag^{2+}} \tag{4}$$

As Ag^{2+} can easily form peroxides in aqueous solutions (eqn (5)), the photocatalytic oxidation of these peroxides might lead to the formation of O_2 (eqn (6)).[50]

$$\mathrm{2Ag^{2+} + 2H_2O \rightarrow Ag_2O_2 + 4H^+} \tag{5}$$

$$\mathrm{2h^+ + Ag_2O_2 \rightarrow 2Ag^{2+} + O_2} \tag{6}$$

The formation of Ag_2O could occur when Ag^+ reacts with oxygen species on the surface, as represented in eqn (7) and (8), and could be reduced to silver nanocomposites.[51]

$$\mathrm{2Ag^+ + O^{2-} \rightarrow Ag_2O} \tag{7}$$

$$\mathrm{Ag_2O \rightarrow AgO + Ag} \tag{8}$$

Nevertheless, the effect of visible-light exposure on the structure of the nanocomposites was evaluated using filtration through centrifuge membranes with different pore sizes (Fig. S1a). The results confirm that the PEP·Na_aAg_b can pass through the 50 kDa NMWL membrane (Amicon® Ultra centrifugal filter, Millipore, Billerica, MA, USA). No peaks were observed in the UV-Vis spectra in the visible region (Fig. S1b), suggesting the presence of Ag^+ ions. In contrast, the silver nanocomposites protected with PPDEs, which were already exposed to visible light, exhibit a peak in the visible region. Furthermore, the residue that could pass through the membrane showed the same peak region as shown in Fig. S1c, providing evidence that the light exposure causes the structural changes occurring in the silver nanocomposites.

After visible-light irradiation, the UV-Vis spectra of PEP·Na_1Ag_1-l, PEP·Na_2Ag_1-l, and PEP·Na_5Ag_1-l were analyzed to investigate their photophysical properties (Fig. 3(a)–(c)). The color of the reaction changed from light yellow to gray/black, confirming the reduction.[52,53] All samples were checked by a V-650 UV-Vis spectrophotometer, which exhibited an absorption peak in the visible region (Fig. 3(a)), especially in the absorption region of silver in the composite, at 407–420 nm.[54] Heterogeneity of silver nanocomposites can significantly enhance visible-light absorption and separate electron–hole pairs, thereby improving photocatalytic activity.[55] The absorbance increased with an increase in Ag concentration, indicating that a higher number of particles were generated as more Ag^+ ions were reduced and transformed into silver nanocomposites.

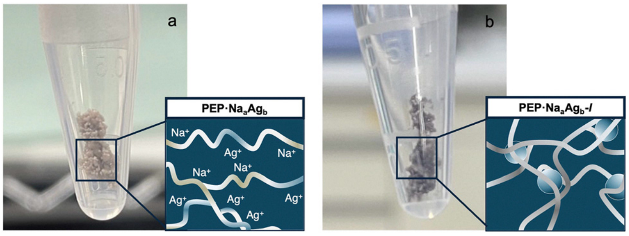

Fig. 2 Schematic of PEP·Na_aAg_b (a) and PEP·Na_aAg_b-l (b).

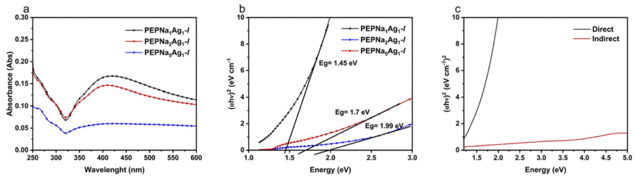

Fig. 3 UV-Vis spectra (a) and Tauc plot (b) of the PEP·Na_1Ag_1-l, PEP·Na_2Ag_1-l, and PEP·Na_5Ag_1-l nanocomposites. Direct and indirect band gap of the PEP·Na_1Ag_1-l (c).

The energy band gaps (E_g) for each sample were estimated by the Tauc plot:

Direct:

$$(\alpha h\nu)^2 = K(h\nu - E_g) \tag{9}$$

Indirect:

$$(\alpha h\nu)^{1/2} = K(h\nu - E_g) \tag{10}$$

where α, $h\nu$, K, and E_g are the absorption coefficient, photon energy, energy-independent constant, and bandgap energy, respectively.

Fig. 3(b) shows the optical direct bandgap determined by the Tauc plot using eqn (9), where the absorbance was obtained from a V-730 UV-Vis spectrophotometer. The bandgap energy (E_g) values of PEP·Na_1Ag_1-l, PEP·Na_2Ag_1-l, and PEP·Na_5Ag_1-l were calculated to be 1.45 eV, 1.7 eV, and 1.99 eV, respectively.[56] These values correspond to the ratio of the PPDEs, with the highest ratio resulting in the least agglomeration. The silver nanocomposites exhibited a bandgap widening due to the quantum confinement effect.[57] As shown in Fig. 3(c), the curve plot compares the direct and indirect band gaps of PEP·Na_1Ag_1-l obtained from eqn (9) and (10), respectively. The distinct work functions of the silver nanocomposites facilitated strong interactions among these components, resulting in broad and tightly bonded interfaces. Schottky barriers and band bending were generated at these interfaces due to the silver nanocomposites, eventually achieving equilibrium at their Fermi levels.[58,59] Thus, the silver nanocomposites are expected to exhibit high photocatalytic abilities.

The micrographs of the synthesized samples are shown in Fig. 4(a)–(d). The TEM images of the PEP·Na_5Ag_1-l show regular spherical-shaped particles with an average size of 10–20 nm (Fig. 4(a)). Based on the dynamic light scattering data shown in Fig. 4(b), the average diameter (Z_{ave}) was estimated to be 176 nm, which is more than that observed using TEM. This difference may be due to the surface functionalization of the polymer layer surrounding the silver nanocomposites, which is

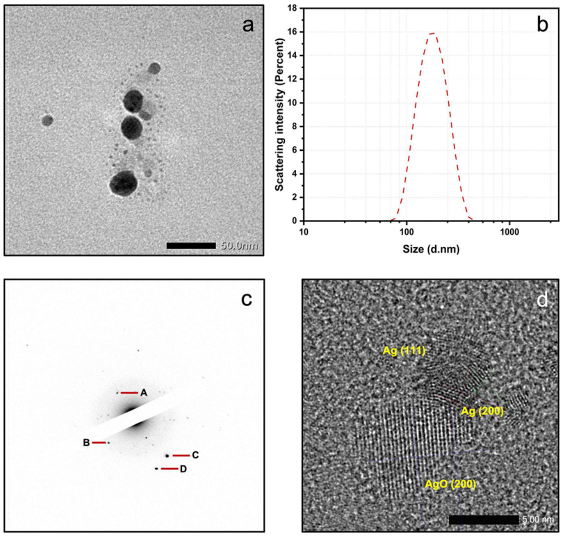

Fig. 4 Transmission electron microscopy images (a), dynamic light scattering measurement (b), selected area electron diffraction patterns (c), and high-resolution TEM images (d) of PEP·Na_5Ag_1-l.

detected by DLS.[60] The corresponding polydispersity index (PDI) was 0.27. The crystalline structure of the silver nanocomposites was analyzed based on SAED patterns and HRTEM images (Fig. 4(c) and (d), respectively). The TEM image and corresponding SAED pattern are shown in Fig. 4(a) and (c). The SAED pattern (Fig. 4(c)) consists of diffraction spots and the halo pattern, suggesting that an amorphous structure was not observed. According to the standard lattice parameter in bulk Ag,[61] AgO,[62] and Ag_2O,[63] the diffraction spot A was indexed as AgO {200}, while the spot B was indexed as Ag {111}. On the other hand, diffraction spot C cannot be determined because the interplanar spacing of Ag_2O {220} (1.6829 Å), AgO (31−1) (1.6993 Å), and AgO (202) (1.6753 Å) are similar. Similarly, diffraction spot D cannot be distinguished because Ag {220} (1.4447 Å) and AgO (220) (1.4759 Å) are very close. Electron diffraction revealed that the silver-based nanocomposite consists of crystalline metallic silver and silver oxide. Fig. 4(d) shows the HRTEM image of a silver-based nanocomposite particle with a complex shape. The upper area shows the multiple twin particle (MTP) structure, which is the typical characteristic structure of noble metal nanoparticles, with interplanar spacings matching those of Ag (111) and (200) planes. In contrast, the lattice fringes observed in the lower areas were indexed as AgO (200) from the spacing.

The surface chemical composition and valence state of the elements of silver nanocomposites were characterized by XPS (Fig. 5(a)–(d)). The complete XPS spectrum reveals the presence of Ag, O, C, Na, and P elements (Fig. 5(a)). The peak of the P_{2p} spectrum is at 133.0 eV, which directly corresponds to the phosphorus (Fig. 5(b)).[64] The deconvoluted XPS spectrum of P_{2p} reveals that the peak at 133 eV constitutes 75–80% of the P_{2p} signal, which can be attributed to the presence of PO_4^{3-} within the polyphosphodiester molecule.[65]

The XPS spectra of Ag_{3d} reveal two distinct peaks, displaying the spin–orbit split lines of $Ag3d_{3/2}$ and $Ag3d_{5/2}$ (Fig. 5(c)).

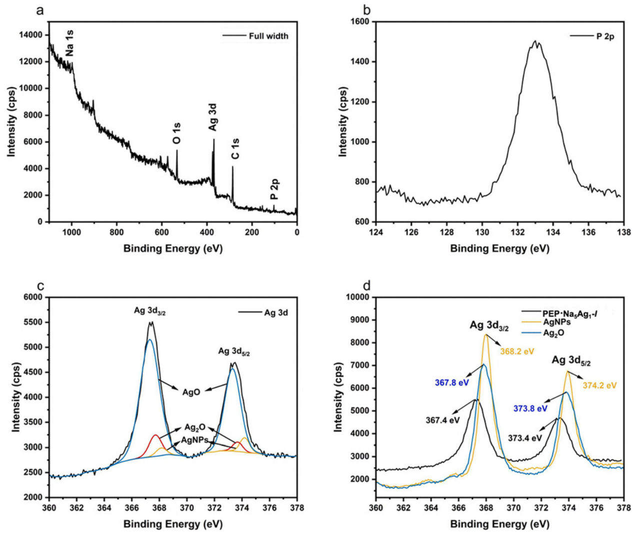

Fig. 5 X-Ray photoelectron spectroscopy full spectrum (a), P_{2p} (b), Ag_{3d} (c). The Ag_{3d} comparison of the PEP·Na_5Ag_1-l, AgNPs, and Ag_2O (d).

PEP·Na_5Ag_1-l displayed peaks at 367.4 eV and 373.4 eV, which can be assigned to the standard Ag_{3d} binding energies of AgO at 367.3 eV and 373.3 eV.[66] The additional peaks observed at 367.8 eV and 373.8 eV can be attributed to Ag ions in the +1 oxidation state of Ag_2O.[67] Furthermore, the peaks at 368.2 eV and 374.2 eV indicate the presence of Ag.[68] The atomic percentages of AgO, Ag_2O, and Ag are 79.2%, 12%, and 8.8%, respectively. Metal oxidation typically results in a shift of binding energy (BE) to higher values due to a reduction in valence electron density. However, in the case of silver, the BE of oxides is lower than that of metallic Ag because of dominant effects such as the Hartree potential.[69] Fig. 5(d) shows the chemical shift of the PEP·Na_5Ag_1-l with the AgNPs and Ag_2O. The results indicate shifts of 0.8 eV and 0.4 eV, which correspond to those observed for AgO with AgNPs and Ag_2O, respectively. These results confirm the presence of the dominant silver state of AgO.

The dispersibility properties of the silver nanocomposites were analyzed (Fig. 6(a)–(b)). As shown in Fig. 6(a), these nanocomposites showed distinct differences in behavior. The commercial AgNPs and Ag_2O powders exhibited significant agglomeration even at low concentrations, while the PEP·Na_5Ag_1-l dispersed more readily. The limited dispersibility of the commercial AgNPs and Ag_2O weakens their photocatalytic efficiency due to reduced interaction with aqueous environments. A comparison of the transmittance (%T) of the PEP·Na_1Ag_1-l, PEP·Na_2Ag_1-l, and PEP·Na_5Ag_1-l revealed a notable trend (Fig. 6(b)). PEP·Na_5Ag_1-l achieved the highest %T, surpassing PEP·Na_2Ag_1-l and PEP·Na_1Ag_1-l, indicating significantly improved dispersibility and transparency. The adsorption of high-molecular-weight charged polymers can induce electrosteric stabilization through a combination of steric hindrance and electrostatic repulsion.[70] These findings underscore that the enhanced dispersibility of the silver nanocomposites arises from the hydrophilic polymer coating layer of PPDEs, which

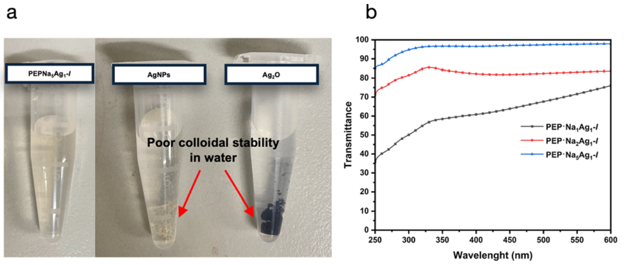

Fig. 6 Photographs of the PEP·Na_5Ag_1-l, AgNPs, and Ag_2O (a). Transmittance (%T) spectra of the PEP·Na_1Ag_1-l, PEP·Na_2Ag_1-l, and PEP·Na_5Ag_1-l (b).

imparts a negative surface charge with a zeta potential of −45.7 mV.

3.2. Photocatalytic activity

Under visible-light irradiation, the photocatalytic performance of silver nanocomposites protected with PPDEs was evaluated at various time points under identical conditions by measuring the degradation efficiency of RhB (Fig. 7(a)–(f)). The maximum absorption at 554 nm, these absorption bands may be attributed to the π–π* transitions of the conjugated molecules.[71] After irradiation, PEP·Na_1Ag_1-l displayed excellent photocatalytic activity at t = 10 minutes (Fig. 7(a)). The absorption at 554 nm immediately decreased with an increase in irradiation time, as indicated by the reddish-violet color and absorption of the RhB solution.[72] Furthermore, the intensity of a new peak at ∼440 nm also increased, which is a characteristic of the absorption of silver nanocomposites. After irradiation for 45 minutes, the absorbance peak shifts to a higher wavelength at 447 nm. The blueshift of the absorbance peak occurs during irradiation time, accompanied by an increase in the particle's size.[73] The degradation of RhB was also evaluated under dark conditions, and no decrease in the 554 nm peak was observed (Fig. 7(b)). PEP·Na_2Ag_1-l followed a similar trend, with a slight reduction in the 554 nm peak, while a new peak around 407–434 nm appeared (Fig. 7(c)). The results show the absorbance peak shifted to a higher wavelength of 434 nm after irradiation for 360 minutes. The lack of the RhB degradation under dark conditions is consistent with PEP·Na_1Ag_1-l (Fig. 7(d)). Furthermore, as shown in Fig. 7(e), the photocatalytic activity of PEP·Na_5Ag_1-l, represented by the peak at 554 nm, decreased slightly compared to that of PEP·Na_1Ag_1-l and PEP·Na_2Ag_1-l. However, the absorbance peak also indicated a blueshift according to irradiation time, as evidenced by a shift to 431 nm after 360 minutes of irradiation. No RhB degradation was observed under dark conditions (Fig. 7(f)). The heterojunctions between silver nanocomposites are critical for photocatalysis, as they enhance visible-light absorption, adjust the geometry and electron structures of the nanocomposites, and reduce recombination of photo-induced electron–hole pairs.[74]

At low dye concentrations, the degradation kinetics of the RhB can be described using the first-order Langmuir equation. A comparison of the initial and final concentrations of each sample is shown in Fig. 7(g). All the samples exhibited higher photocatalytic activity than RhB irradiated by visible light.

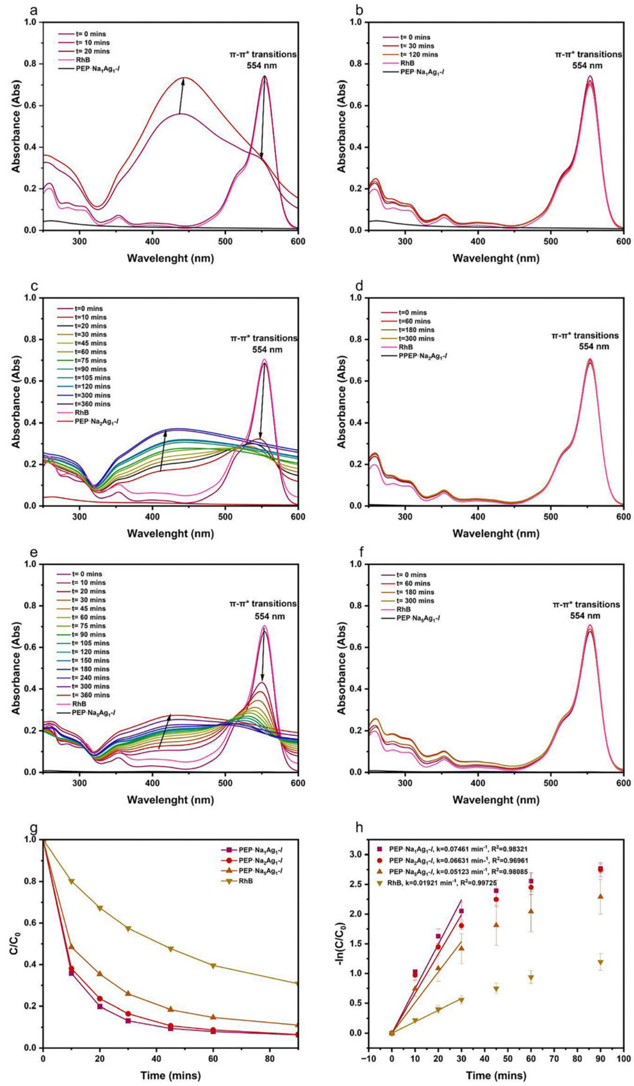

Fig. 7 UV-Vis spectra showing RhB degradation by PEP·Na_1Ag_1-l (a), (b), PEP·Na_2Ag_1-l (c), (d), and PEP·Na_5Ag_1-l (e), (f) under visible light and dark conditions, respectively. The C/C_0 ratio (g), and first-order kinetics of PEP·Na_1Ag_1-l, PEP·Na_2Ag_1-l, PEP·Na_5Ag_1-l, and the control sample are also shown (h).

The PEP·Na_1Ag_1-l demonstrated the highest photocatalytic activity, capable of removing approximately 94% of RhB after 90 minutes. The PEP·Na_2Ag_1-l and PEP·Na_5Ag_1-l samples also demonstrated high activity, removing 93.5% and 89% of RhB, respectively. The apparent reaction rate constant (k) was determined from the initial linear region (0–30 min) of the $-\ln(C/C_0)$ *versus* time plot (Fig. 7(h)). After 30 minutes of irradiation, the RhB concentration becomes sufficiently low, leading to deviations from ideal pseudo-first-order linearity as shown in Fig. S2. Therefore, the kinetic reaction rate was determined using data from the initial stage (0–30 min), where the reaction is described by a pseudo-first-order model. As the error bars represent the standard error of mean (n = 3). The calculated k values (t = 0 to 30 min) obtained 7.46×10^{-2}, 6.63×10^{-2}, and 5.12×10^{-2} min^{-1} for PEP·Na_1Ag_1-l, PEP·Na_2Ag_1-l, and

PEP·Na_5Ag_1-l, respectively. The reaction rate constant of PEP·Na_1Ag_1-l was more than three times that of the control sample, indicating that the presence of silver nanocomposites in PPDEs enables photocatalytic activity under visible light. The photocatalytic reaction rate constants under visible light of the silver-based photocatalyst were compared to those previously reported, as shown in Table S1. Obviously, our study exhibits an exceptional reaction rate constant compared with previous reports. Thus, the photocatalytic performance of the silver nanocomposites protected with PPDEs is remarkably under visible light, even without coupling with conventional semiconductor-based photocatalysts (*e.g.*, TiO_2, ZnO).

The proposed photocatalytic mechanism for RhB degradation by silver nanocomposites is explained using a schematic (Fig. 8). Under visible-light exposure, electrons in the valence band (VB) of the silver nanocomposites are excited to the conduction band (CB), leaving behind holes in the VB. The CB potentials of Ag_2O (−0.31 eV) and AgO (0.72 eV) are well-aligned to facilitate electron transfer.[75] As the CB potential of AgO is more positive than that of Ag_2O, photogenerated electrons from Ag_2O can transfer to the CB of AgO and then to the Fermi level of Ag (0.99 eV), which acts as an electron sink. Photogenerated holes can migrate due to the more negative VB potential of Ag_2O (0.54 eV) compared to AgO (1.84 eV), creating a gradient that facilitates the accumulation of holes in Ag_2O, which are highly active in oxidation reactions.[76]

The heterojunction structure of silver nanocomposites enabled the efficient transfer of electrons and holes across different components, creating a multichannel charge transfer pathway. This mechanism effectively prevents charge recombination, prolongs the lifetime of reactive charges, and enhances photocatalytic activity. The Ag in the nanocomposite acts as a plasmonic center, enabling the absorption of visible light through localized surface plasmon resonance. This increases the generation of photogenerated carriers as well as facilitates their transfer within the heterojunction network.

In this study, the predominance of h^+ and $O_2^{-\bullet}$ radicals causes the stepwise degradation of RhB into CO_2, H_2O, and other byproducts, as shown in eqn (11)–(14). Further studies should focus on optimizing the content and distribution of silver nanocomposites to enhance charge separation in the multichannel.

The reactive oxygen species (ROS), such as holes (h^+), hydroxyl free radicals ($OH^\bullet$), and superoxide anion free radicals ($O_2^{-\bullet}$), are generated during optical excitation. During photocatalytic tests, specific scavengers were added to the RhB solutions under visible light to help identify the main ROS species responsible for degradation. The scavengers used for h^+, $OH^\bullet$, and $O_2^{-\bullet}$ radicals were triethanolamine (TEOA), 2-propanol, and *p*-benzoquinone (*p*-BQ), respectively.

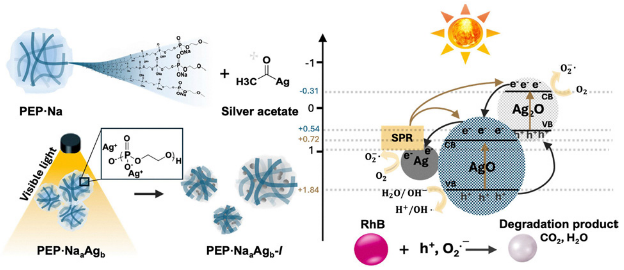

Fig. 8 Schematic representation of the photocatalytic mechanism of silver nanocomposites.

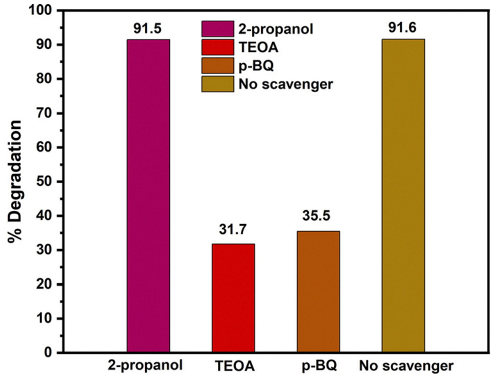

Fig. 9 Free radical scavenger test of PEP·Na_5Ag_1-l. The h^+, $OH^\bullet$, and $O_2^{-\bullet}$ radicals were removed using triethanolamine (TEOA), 2-propanol, and *p*-benzoquinone (*p*-BQ), respectively. The control sample did not have any scavengers.

Fig. 9 shows the photodegradation efficiency of the PEP·Na_5Ag_1-l with different scavengers and a control sample without any scavenger. The photodegradation efficiency of the PEP·Na_5Ag_1-l in RhB dye removal after 90 minutes of visible light exposure, with the addition of TEOA, 2-propanol, *p*-BQ, and no scavenger, was 31.7%, 91.5%, 35.5%, and 91.6%, respectively. Introducing these scavengers decreased both degradation rate and photocatalytic activity, indicating that two ROS contribute significantly to degradation (h^+ and $O_2^{-\bullet}$). The result shows that holes (h^+) have the greatest impact on this process, highlighting their predominant role in driving photocatalytic efficiency.

The potential reactions involved in the photocatalytic degradation of the samples are outlined below.[77]

$$Ag/AgO/Ag_2O + h\nu \rightarrow h^+_{(VB)} + e^- \tag{11}$$

$$e^- + O_2 \rightarrow O_2^{-\bullet} \tag{12}$$

$$RhB + h^+_{(VB)} \rightarrow \text{degradation products.} \tag{13}$$

$$RhB + O_2^{-\bullet} \rightarrow \text{degradation products} \tag{14}$$

Understanding the role of the silver nanocomposites as stable and efficient photocatalysts under visible light irradiation is essential for advancing photocatalytic applications. Fig. 10 shows the photocatalytic performance of PEP·Na_5Ag_1-l, which degraded over 87% of the RhB dye after six cycles. As the ratio of the PPDEs influences the dispersibility, it also impacts the recyclability. Therefore, the PEP·Na_5Ag_1-l, which has a high ratio of PPDEs, exhibits consistent photocatalytic performance over repeated cycles by maintaining an active interface for ongoing ROS generation.

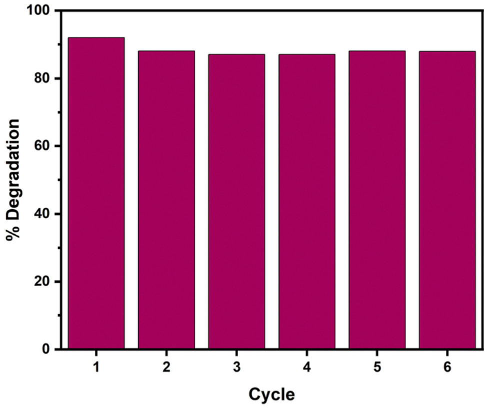

Fig. 10 Recyclability of the PEP·Na_5Ag_1-l.

4. Conclusions

In this study, we designed and synthesized silver nanocomposites protected with PPDEs from unsaturated silver salts of PPDEs. The silver nanocomposites were formed *via* visible-light irradiation. The coexistence of PPDEs and silver nanocomposites was confirmed by different characterization techniques. The TEM/HRTEM images, SAED patterns, and XPS spectra revealed that the silver nanocomposites consist of Ag, AgO, and Ag_2O. Furthermore, these PEP·Na_1Ag_1-l, PEP·Na_2Ag_1-l, and PEP·Na_5Ag_1-l nanocomposites exhibited exceptional photocatalytic performance under visible light irradiation, achieving 94%, 93.5%, and 89% RhB degradation efficiency, respectively, within 90 minutes. Their reaction rate constants (*k* values) of 7.46×10^{-2}, 6.63×10^{-2}, and 5.12×10^{-2} min^{-1}, respectively, represent a significant enhancement over the control sample. PEP·Na_5Ag_1-l showed the highest dispersibility, colloidal stability, and recyclability due to its elevated PPDE content. This nanocomposite retained over 87% RhB degradation efficiency even after six cycles, showing its high recyclability. The high photocatalytic efficiency of this system was driven by specific (h^+ and $O_2^{-\bullet}$), with the heterojunction structure enhancing charge transfer and suppressing electron–hole recombination.

Author contributions

Thanaporn Jullabuth: methodology, formal analysis, investigation, writing – original draft, writing – review and editing. Yota Okuno: investigation, formal analysis. Hideya Kawasaki: methodology, data curation. Satoshi Ichikawa: investigation, writing – review & editing. Yasuhiko Iwasaki: conceptualization, formal analysis, funding acquisition, resources, supervision, writing – original draft, writing – review & editing.

Conflicts of interest

There are no conflicts to declare.

Data availability

The data supporting this article have been included as part of the supplementary information (SI). Supplementary information is available. See DOI: https://doi.org/10.1039/d5ma01295c.

Acknowledgements

This work was supported by the Ministry of Trade, Industry and Energy (MOTIE) of Korea (grant no. 20018324) and KAKENHI from the Japan Society for the Promotion of Science (#23H03750).

References

1 T. Ochiai and A. Fujishima, *J. Photochem. Photobiol., C*, 2012, **13**, 247–262.
2 C. Yu, W. Zhou, H. Liu, Y. Liu and D. D. Dionysiou, *Chem. Eng. J.*, 2016, **287**, 117–129.
3 J. Li, W. Fang, C. Yu, W. Zhou, L. Zhu and Y. Xie, *Appl. Surf. Sci.*, 2015, **358**, 46–56.
4 C.-M. Fung, C.-C. Er, L.-L. Tan, A. R. Mohamed and S.-P. Chai, *Chem. Rev.*, 2022, **122**, 3879–3965.
5 W. Li, M. Sohail, U. Anwar, T. A. Taha, A. G. Al-Sehemi, S. Muhammad, A. A. Al-Ghamdi, M. A. Amin, A. Palamanit, S. Ullah, A. Hayat and Z. Ajmal, *Int. J. Hydrogen Energy*, 2022, **47**, 21067–21118.
6 M. Z. A. Warshagha and M. Muneer, *ACS Omega*, 2022, **7**, 30171–30183.
7 Y. Ohko, Y. Utsumi, C. Niwa, T. Tatsuma, K. Kobayakawa, Y. Satoh, Y. Kubota and A. Fujishima, *J. Biomed. Mater. Res.*, 2001, **58**, 97–101.
8 A. Subrahmanyam, P. R. Thangaraj, C. Kanuru, A. Jayakumar and J. Gopal, *Med. Eng. Phys.*, 2014, **36**, 530–533.
9 D. Pathania, M. Kumari and V. K. Gupta, *Mater. Des.*, 2015, **87**, 1056–1064.
10 A. Fujishima and K. Honda, *Nature*, 1972, **238**, 37–38.
11 T. Zhu and S.-P. Gao, *J. Phys. Chem. C*, 2014, **118**, 11385–11396.
12 A. L. Linsebigler, G. Lu and J. T. Yates, *Chem. Rev.*, 1995, **95**, 735–758.
13 S. Sarina, E. R. Waclawik and H. Zhu, *Green Chem.*, 2013, **15**, 1814.
14 W. Xue, D. Huang, X. Wen, S. Chen, M. Cheng, R. Deng, B. Li, Y. Yang and X. Liu, *J. Hazard. Mater.*, 2020, **390**, 122128.
15 R. K. Sharma, S. Yadav, S. Dutta, H. B. Kale, I. R. Warkad, R. Zbořil, R. S. Varma and M. B. Gawande, *Chem. Soc. Rev.*, 2021, **50**, 11293–11380.
16 M. Maraj, H. Anwar, A. Saba, G. Nabi, N. Shaheen, N. Ansar, W. Ali, A. Fatima, A. Raza and W. Sun, *Arabian J. Chem.*, 2023, **16**, 104906.
17 D. Vidyasagar, S. G. Ghugal, A. Kulkarni, P. Mishra, A. G. Shende, J. Jagannath, S. S. Umare and R. Sasikala, *Appl. Catal., B*, 2018, **221**, 339–348.

18 W. Xu, S. Q. Wang, Q. Y. Zhang, C. Y. Ma, Q. Wang, D. H. Wen and X. N. Li, *J. Alloys Compd.*, 2019, **802**, 210–216.
19 W. Jiang, X. Wang, Z. Wu, X. Yue, S. Yuan, H. Lu and B. Liang, *Ind. Eng. Chem. Res.*, 2015, **54**, 832–841.
20 B. N. Rashmi, S. F. Harlapur, B. Avinash, C. R. Ravikumar, H. P. Nagaswarupa, M. R. Anil Kumar, K. Gurushantha and M. S. Santosh, *Inorg. Chem. Commun.*, 2020, **111**, 107580.
21 S. Meng, D. Li, X. Fu and X. Fu, *J. Mater. Chem. A*, 2015, **3**, 23501–23511.
22 H. Xu, J. Xie, W. Jia, G. Wu and Y. Cao, *J. Colloid Interface Sci.*, 2018, **516**, 511–521.
23 M. Humayun, C. Wang and W. Luo, *Small Methods*, 2022, **6**, 2101395.
24 R. E. Adam, E. Chalangar, M. Pirhashemi, G. Pozina, X. Liu, J. Palisaitis, H. Pettersson, M. Willander and O. Nur, *RSC Adv.*, 2019, **9**, 30585–30598.
25 N. Ben Saber, A. Mezni, A. Alrooqi and T. Altalhi, *J. Mater. Res. Technol.*, 2020, **9**, 15233–15262.
26 A. Bansal, S. Madhavi, T. T. Y. Tan and T. M. Lim, *Catal. Today*, 2008, **131**, 250–254.
27 C. Ren, B. Yang, M. Wu, J. Xu, Z. Fu, Y. Lv, T. Guo, Y. Zhao and C. Zhu, *J. Hazard. Mater.*, 2010, **182**, 123–129.
28 Y. Cui, Q. Ma, X. Deng, Q. Meng, X. Cheng, M. Xie, X. Li, Q. Cheng and H. Liu, *Appl. Catal., B*, 2017, **206**, 136–145.
29 C. Liang, H. Guo, L. Zhang, M. Ruan, C.-G. Niu, H.-P. Feng, X.-J. Wen, N. Tang, H.-Y. Liu and G.-M. Zeng, *Chem. Eng. J.*, 2019, **372**, 12–25.
30 R. Dong, B. Tian, C. Zeng, T. Li, T. Wang and J. Zhang, *J. Phys. Chem. C*, 2013, **117**, 213–220.
31 P. Hu, Y. Cao, D. Jia, Q. Li and R. Liu, *Sci. Rep.*, 2014, **4**, 4153.
32 Y. Liu, L. Fang, H. Lu, L. Liu, H. Wang and C. Hu, *Catal. Commun.*, 2012, **17**, 200–204.
33 M. Barwant, Y. Ugale, S. Ghotekar, P. Basnet, V.-H. Nguyen, S. Pansambal, H. C. A. Murthy, T.-D. Pham, M. Bilal, R. Oza and V. Karande, *Research Square*, 2021, DOI: 10.21203/rs.3.rs-973781/v1.
34 M. Feng, M. Zhang, J.-M. Song, X.-G. Li and S.-H. Yu, *ACS Nano*, 2011, **5**, 6726–6735.
35 Y. Yang, Y. Guo, F. Liu, X. Yuan, Y. Guo, S. Zhang, W. Guo and M. Huo, *Appl. Catal., B*, 2013, **142–143**, 828–837.
36 Y. Iwasaki, *Molecules*, 2020, **25**, 758.
37 A. Cankaya, M. Steinmann, Y. Bülbül, I. Lieberwirth and F. R. Wurm, *Polym. Chem.*, 2016, **7**, 5004–5010.
38 Y. Hirano and Y. Iwasaki, *Colloids Surf., B*, 2017, **153**, 104–110.
39 A. Otaka and Y. Iwasaki, *J. Ind. Eng. Chem.*, 2019, **75**, 115–122.
40 S. Kootala, M. Tokunaga, J. Hilborn and Y. Iwasaki, *Macromol. Biosci.*, 2015, **15**, 1634–1640.
41 S. Noree and Y. Iwasaki, *ACS Omega*, 2019, **4**, 3398–3404.
42 K. Kiyono, S. Mabuchi, A. Otaka and Y. Iwasaki, *J. Biomed. Mater. Res.*, 2023, **111**, 714–724.
43 Y. Seto and M. Ohtsuka, *J. Appl. Crystallogr.*, 2022, **55**, 397–410.
44 J. Wang, H.-Q. Mao and K. W. Leong, *J. Am. Chem. Soc.*, 2001, **123**, 9480–9481.
45 A. Otaka, K. Kiyono and Y. Iwasaki, *Materialia*, 2021, **15**, 100977.
46 M. Barwant, Y. Ugale, S. Ghotekar, P. Basnet, V.-H. Nguyen, S. Pansambal, H. C. Ananda Murthy, M. Sillanpaa, M. Bilal, R. Oza and V. Karande, *Chem. Pap.*, 2022, **76**, 4309–4321.
47 C. An, S. Wang, Y. Sun, Q. Zhang, J. Zhang, C. Wang and J. Fang, *J. Mater. Chem. A*, 2016, **4**, 4336–4352.
48 W. Xue, D. Huang, X. Wen, S. Chen, M. Cheng, R. Deng, B. Li, Y. Yang and X. Liu, *J. Hazard. Mater.*, 2020, **390**, 122128.
49 T. H. Jeon, D. Monllor–Satoca, G. Moon, W. Kim, H. Kim, D. W. Bahnemann, H. Park and W. Choi, *Nat. Commun.*, 2020, **11**, 967.
50 J. Schneider and D. W. Bahnemann, *J. Phys. Chem. Lett.*, 2013, **4**, 3479–3483.
51 X. Wang, S. Li, H. Yu, J. Yu and S. Liu, *Chem. – Eur. J.*, 2011, **17**, 7777–7780.
52 A. L. González, C. Noguez, J. Beránek and A. S. Barnard, *J. Phys. Chem. C*, 2014, **118**, 9128–9136.
53 A. Rita, A. Sivakumar, S. S. J. Dhas and S. A. M. B. Dhas, *J. Nanostruct. Chem.*, 2020, **10**, 309–316.
54 K. Deekshitha and V. Shetty K, *Mater. Sci. Semicond. Process.*, 2021, **132**, 105923.
55 G. S. Lekshmi, R. Tamilselvi, R. Geethalakshmi, S. D. Kirupha, O. Bazaka, I. Levchenko, K. Bazaka and M. Mandhakini, *J. Colloid Interface Sci.*, 2022, **608**, 294–305.
56 M. Padilla Villavicencio, A. Escobedo Morales, Ma. D. L. Ruiz Peralta, M. Sánchez-Cantú, L. Rojas Blanco, E. Chigo Anota, J. H. Camacho García and F. Tzompantzi, *Catal. Lett.*, 2020, **150**, 2385–2399.
57 A. J. Das, R. Kumar, S. P. Goutam and S. S. Sagar, *J. Bioeng. Biomed. Sci.*, 2016, **6**(5), 1000208.
58 S. Ma, J. Xue, Y. Zhou and Z. Zhang, *J. Mater. Chem. A*, 2014, **2**, 7272–7280.
59 Y. Peng, H. Zhou, Z. Ma, L. Tian, R. Zhang, H. Tu and L. Jiang, *Int. J. Biol. Macromol.*, 2023, **225**, 185–197.
60 U. Chatterjee, S. K. Jewrajka and S. Guha, *Polym. Compos.*, 2009, **30**, 827–834.
61 R. W. G. Wyckoff, *Cryst. Struct.*, 1963, **1**, 7–83.
62 R. W. G. Wyckoff, *Cryst. Struct.*, 1963, **1**, 85–237.
63 R. W. G. Wyckoff, *Am. J. Sci.*, 1922, **3**, 184–188.
64 B. Wang, J. Liu, Q. Sun, R. Li, T.-K. Sham and X. Sun, *Nanotechnology*, 2014, **25**, 504007.
65 H. Hassan, M. W. Iqbal, N. H. Al-Shaalan, S. Alharthi, N. D. Alqarni, M. A. Amin and A. M. Afzal, *Nanoscale Adv.*, 2023, **5**, 4735–4751.
66 Y. Ida, S. Watase, T. Shinagawa, M. Watanabe, M. Chigane, M. Inaba, A. Tasaka and M. Izaki, *Chem. Mater.*, 2008, **20**, 1254–1256.
67 S. Aravindan, V. Rajendran and N. Rajendran, *Phase Transitions*, 2012, **85**, 630–649.
68 N. J. Firet, M. A. Blommaert, T. Burdyny, A. Venugopal, D. Bohra, A. Longo and W. A. Smith, *J. Mater. Chem. A*, 2019, **7**, 2597–2607.

69 G. Schön, J. Tummavuori, B. Lindström, C. R. Enzell, C. R. Enzell and C.-G. Swahn, *Acta Chem. Scand.*, 1973, **27**, 2623–2633.

70 S. Lin, Y. Cheng, J. Liu and M. R. Wiesner, *Langmuir*, 2012, **28**, 4178–4186.

71 A. Udrescu, S. Florica, M. Chivu, I. Mercioniu, E. Matei and M. Baibarac, *Molecules*, 2021, **26**, 7237.

72 H. Liang, S. Liu, H. Zhang, X. Wang and J. Wang, *RSC Adv.*, 2018, **8**, 13625–13634.

73 J. Cao, T. Sun and K. T. V. Grattan, *Sens. Actuators, B*, 2014, **195**, 332–351.

74 L. Zhou, G. Zou and H. Deng, *Catalysts*, 2018, **8**, 272.

75 H. Bian, Z. Zhang, X. Xu, Y. Gao and T. Wang, *Phys. E*, 2020, **124**, 114236.

76 W. Shen, X. Wang, Y. Ge, H. Feng and L. Feng, *Colloids Surf., A*, 2019, **575**, 102–110.

77 A. Sobhani-Nasab and M. Behpour, *J. Mater. Sci.: Mater. Electron.*, 2016, **27**, 1191–1196.